# Spin Hall effect induced by strain coupling of valley and spin polarization in puckered monochalcogenide tellurene monolayer

Parrydeep Kaur Sachdeva,[1,2,3] Shuchi Gupta,[2] and Chandan Bera[1,*]

[1]*Institute of Nano Science and Technology, Sector-81, Knowledge City, Sahibzada Ajit Singh Nagar, Punjab 140306, India*
[2]*University Institute of Engineering and Technology, Panjab University, Sector-25, Chandigarh 160014, India*
[3]*Department of Physics, Panjab University, Sector-14, Chandigarh 160014, India*

(Received 31 August 2022; revised 22 March 2023; accepted 6 April 2023; published 18 April 2023)

Spin-orbit coupling (SOC) and spatial inversion asymmetry are together capable of hosting a variety of effects such as Rashba and SOC spin splittings accompanied with Berry phase effects. Predominantly, spin-valley coupling and valley-contrasting physics are studied in hexagonal transition-metal dichalcogenides. In this work, we explore monoclinic monochalcogenide tellurene monolayer in two stable phases ($\beta$ and $\beta'$) for strain coupled spin-valleytronic properties using first-principles calculations. A high Rashba coefficient of 0.90 eVÅ is obtained in strained $\beta$-Te while it magnifies to 1.55 eV Å at 8% strain in $\beta'$-Te. Time-reversal-connected valleys in tellurene lead to an induced Berry curvature (BC) in $\beta$-Te by the application of strain. The strain-induced BC of 21.27 Bohr$^2$ is obtained, specifically at 4.5% biaxial strain in $\beta$-Te by undergoing a phase transition, whereas noncentrosymmetric $\beta'$-Te has a maximum BC of 22.90 Bohr$^2$ at $-4$% strain. Large Rashba spin splittings with spin Berry curvature lead to intrinsically large spin Hall conductivity (SHC) in tellurene. Strain tunable SHC of $\sim$44 $(\hbar/e)$ S/cm is obtained for $p$-type $\beta'$-Te at carrier concentration $n_h \approx 1.1 \times 10^{15}$ cm$^{-2}$, and SHC of $\sim$3.68 $(\hbar/e)$ S/cm is obtained for $n$-type $\beta'$-Te at $n_e \approx 2.3 \times 10^{13}$ cm$^{-2}$. Moreover, finite SHC of 2.48 $(\hbar/e)$ S/cm and two pairs of edge states crossing in the forbidden region implies inversion asymmetric $\beta'$ tellurene as a potential double quantum spin Hall insulator. The comprehensive study of the mentioned intriguing properties of tellurene indicates its high technological potential in a merged spin-valleytronic multifunctional nanodevice and in low-power quantum electronics.

DOI: 10.1103/PhysRevB.107.155420

## I. INTRODUCTION

The collective exploitation of spin orientations and valley degree of freedom of charge carriers in two-dimensional (2D) materials is a novel approach in nanodevice design for integrating spintronic and valleytronic functionalities. 2D materials with broken inversion symmetry and large spin-orbit coupling are profound choices for manifesting the two phenomena of spin and valley manipulation in a material. Although the field of valleytronics is relatively new, both spintronics and valleytronics are emerging fields in the nanoelectronics regime and require constant groundwork and assessment. Controlling valley polarization in time-reversal connected valleys has become an ultramodern approach for information encoding-decoding [1,2]. $MoS_2$ monolayer serves as the epitome of valleytronics in two dimensions wherein valley polarization has been demonstrated experimentally through optical pumping [3,4]. This creates disproportionate carrier concentrations in the inequivalent valleys by selective optical excitation of carriers. The intervalley scattering is expected to be less as the valleys are largely distant in the momentum space. Diversified approaches have been utilized to obtain valley polarization such as external magnetic field, magnetic doping, proximity effect, vacancies, and heterostructure construction [5–8].

In the context of potential application in spintronics, initially magnetic materials have been explored [9–13]. However, there has been a subsequent shift towards manipulating spin degree of freedom in nonmagnetic materials. TMDCs such as $MoX_2$, $WX_2$ ($X$ = S,Se,Te), $TaTe_2$, $PtTe_2$, and perovskite such as $KTaO_3$ [14] are not ferromagnetic by nature, but it is the presence of large spin-orbit coupling that makes them potential candidates for spintronics [15–17]. Incorporation of SOC leads to Rashba-type and SOC-induced spin splittings that lift the spin degeneracy by an intrinsic electric field present in asymmetric materials. These materials are used as the spin channel for spin manipulation and transportation in conjunction with ferromagnetic materials at the source and drain of a spin FET [18]. Giant Rashba and SOC spin splittings are useful in miniaturized spintronic device construction such that large spin-momentum locking leads to shorter spin channels where the spin precesses by 180° at the channel end [19]. The idea of utilizing nonmagnetic materials having significant SOC and spin-momentum locking strength widens up the range of materials that can be employed in spintronics.

The valley and spin polarizations pave the way for valley-dependent carrier transport and quantum effects such as the valley Hall effect [20,21], the anomalous Hall effect [22,23], and the spin Hall effect [15,24]. These effects are governed

*chandan@inst.ac.in

 

by the presence of Berry curvature and spin Berry curvature (SBC). The spin Hall effect emerges from the spin Berry curvature and the strong SOC, which causes spin splitting in the material. The quantum spin Hall effect (QSHE) can be observed in materials having insulating bulk but conducting helical edge states. These spin edge states are topologically protected from scattering by the time-reversal symmetry and thereby they can transfer information without any data loss in quantum devices. QSHE has been found in graphene [25], $1T'$ TMDCs [26,27], $\alpha$-Sb, and $\alpha$-Bi [28]. The concurrence of spintronic and valleytronic properties in a material is desirable for a multifunctional nanoelectronic device. Xiao *et al.* [29] reported and discussed coupling of spin and valley physics in $MoS_2$ monolayer, as well as predicting the occurrence of spin and valley Hall effects in the monolayer.

The interplay of spin and valley properties in 2D materials can be controlled and tuned by strain easily due to their inherent flexibility. Strain has the potential to reduce spatial symmetries of a system and can induce noncentrosymmetry in an initially inversion-symmetric material, thereby inducing spin splitting and Berry curvature dipole and modulating spin and valley polarizations present in 2D compounds. Spin and valley splittings are derived from electronic band structure, which alters dramatically with strain. Strain engineering has proved to be an effective method to enhance and achieve desirable spin-valley splittings and the corresponding Hall effects. Moreover, the manufacturing process of materials causes unavoided strain in the lattice, which compels us to investigate the effect of strain on the physical properties. Son *et al.* [30] demonstrated strain tuned Berry curvature dipole and valley magnetization in $MoS_2$. Slawinska *et al.* [31] discussed the effect of strain on spin Hall conductivities of group-IV monochalcogenides.

Strain has become a medium to provoke the evolution of properties that are generally absent in the material. Recently, strain-induced piezoelectricity arising due to the breakage of inversion symmetry in initially centrosymmetric $\beta$-Te was studied in our previous work [32]. Tellurene monolayer was first predicted by Zhu *et al.* [33], and then synthesized experimentally a few years later using various chemical and mechanical methods [34,35]. Wang *et al.* [35] fabricated tellurene field-effect transistor (FET) with a high on/off ratio of the order of $10^6$. This switching ratio can be expected to be enhanced further by using a spin degree of freedom of tellurene in a spin-FET.

In this study, the potential of monochalcogenide tellurene in coupled spin-valley physics is assessed. Tellurene possesses four important ingredients: (i) lattice inversion asymmetry in one of its phases or producible in strained conditions, (ii) strong spin-orbit coupling due to heavy Te atoms, (iii) energy degenerate multivalleys that can be distinguished in momentum space, and (iv) time-reversal symmetry. These factors are responsible for generating large Rashba and SOC spin splittings as well as valley-contrasting Berry curvature and spin Berry curvature, essential for spintronics and valleytronics. In this regard, the Rashba spin splitting and spin Berry curvature induced significant double quantum spin Hall effect is found in tellurene monolayer. It is also found that tellurene is a merger of spintronic and valleytronic properties so as to have the best of both worlds in this single 2D material. Contemporary electronics is being replaced by spin-valley-tronics, and so the quest to find novel materials for spin-valley-tronics has intensified. Our study will promote experimental investigation of 2D tellurene for extracting quantum Hall effects. The duo of strain and carrier doping has been employed to obtain the optimal spin Hall effect.

## II. COMPUTATIONAL METHOD

In this work, Vienna Ab-initio Simulation Package (VASP) [36] has been used to execute density functional theory (DFT) calculations such as geometric relaxation and electronic band structure. These first-principles calculations are performed with projector augmented waves (PAWs) [37,38] in the generalized-gradient approximation (GGA) [39]. The Perdew-Burke-Ernzerhof (PBE) [40] functional has been used to describe electron exchange and correlation effects. The tellurene monolayer is optimized by allowing its degrees of freedom (ionic positions and cell shape) to change until the Hellmann-Feynman forces on each atom are less than 0.01 eV/Å. The kinetic-energy cutoff for the plane-wave basis is fixed at 400 eV, and the maximum permissible energy difference for proper convergence in electronic relaxation is set at $10^{-8}$ eV. The Brillouin zone is sampled with $14 \times 14 \times 1$ Γ-centered $k$-mesh. Monolayer has a vacuum of approximately 15 Å in the $z$-direction so as to decouple the periodic layers, thus eliminating the factitious interactions between them. The SOC-based electronic band structures have been calculated using two different first-principles codes, VASP and QUANTUM ESPRESSO [41], and they are found to be consistent with each other. Spin-orbit coupling is incorporated in the electronic band-structure calculations to study the Rashba effect and SOC spin splitting in valence and conduction bands. The maximally localized Wannier functions (MLWFs) are used to determine Berry curvatures using WANNIER90 [42,43] code in conjunction with the QUANTUM ESPRESSO package. The Wannier functions are obtained for 12 bands for three Te-atoms per unit cell. These bands are doubled to 24 in order to consider two spins per channel for SOC inclusion. The bands in tellurene are mainly composed of a $p$-orbital with a small contribution from an $s$-orbital. The $sp^3$ hybridized orbitals are used as the initial projections for calculating Berry curvature. These calculation details reconcile with the ones mentioned by Tsirkin *et al.* [44]. The edge-state band-structure calculations are performed using WANNIER TOOLS [45], which used MLWF based on a tight-binding model, constructed from the WANNIER90 package.

Berry curvature $\Omega_{z,n}(k)$ of the $n$th Bloch band at a particular $k$ point is given by the Kubo formula [46,47],

$$\Omega_{z,n}(k) = \Sigma_{n' \neq n} \frac{-2\,\mathrm{Im}[\langle \psi_{nk}|\hat{v}_x|\psi_{n'k}\rangle\langle\psi_{n'k}|\hat{v}_y|\psi_{nk}\rangle]}{(E_n - E_{n'})^2}, \quad (1)$$

where $\hat{v}_{x,y}$ is the velocity operator, $\psi_{nk}$ is the $n$th eigenstate at a $k$ point with eigenvalue, and $E_n = \hbar\omega_{kn}$.

Berry curvature of all the occupied states can be written as the summation of Berry curvature of each band,

$$\Omega_z(k) = \Sigma_n f_n(k)\Omega_{z,n}(k). \quad (2)$$

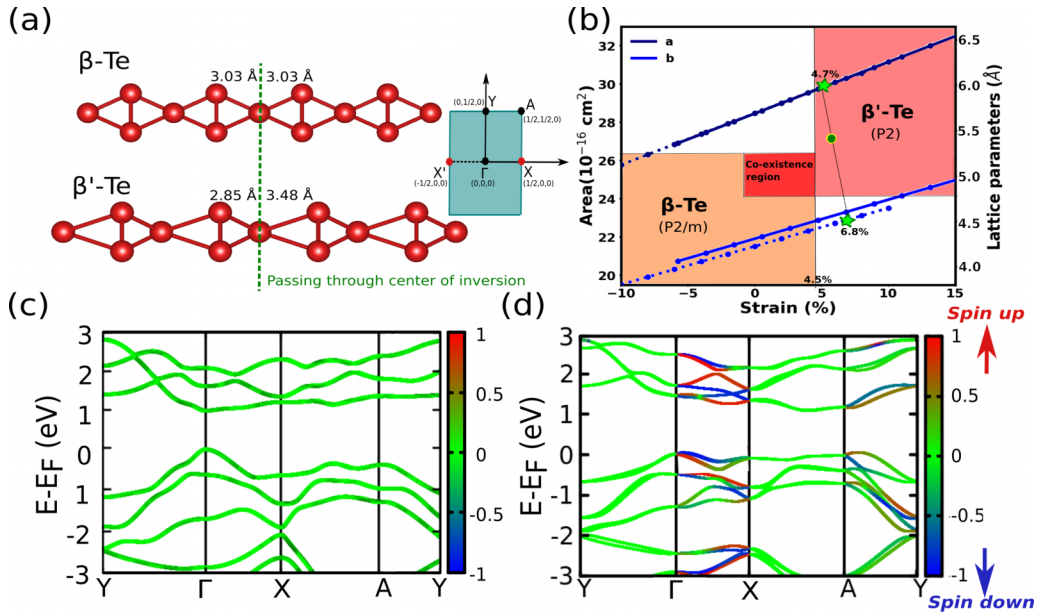


FIG. 1. (a) Side view geometric representations of $\beta$-Te and $\beta'$-Te monolayers using a ball stick model. The plane (in green) passing through the center of inversion clearly depicts the inversion symmetry in $\beta$-Te having same bond lengths on either side of the plane and broken inversion symmetry in $\beta'$-Te as different bond lengths exist between Te-Te atoms; a schematic representation of a 2D Brillouin zone of a monoclinic lattice with labeled high-symmetry $k$ points. (b) Variation of area and lattice parameters of $\beta$-Te and $\beta'$-Te with strain, representing explicit as well as coexistence regions of the two phases. Blue dotted lines represent the parameters "$a$" and "$b$" of $\beta$-Te, while the solid lines are for the lattice parameters of $\beta'$-Te (specific lattice parameters of $\beta'$-Te are marked with green stars, and area is marked with a green circle). (c),(d) Spin-resolved electronic band structures of $\beta$-Te and $\beta'$-Te for the closed path $Y$-$\Gamma$-$X$-$A$-$Y$ using PBE and SOC. The colorbar indicates red for spin-up and blue for spin-down contributions.

Berry curvature is a physical property deduced from the energy-momentum relationship of electrons in asymmetric materials.

The spin Hall effect is the transport phenomenon governed by the spin Berry curvature. So, spin Hall conductivity can be written in terms of spin Berry curvature $\Omega_z^s(k)$ as [48]

$$\sigma_{xy}^{\mathrm{SHC}} = \frac{e}{\hbar}\Sigma_k \Omega_z^s(k) = \frac{e}{\hbar}\Sigma_k \Sigma_n f_n(k)\Omega_{z,n}^s(k), \tag{3}$$

where $f_n$(k) describes the Fermi distribution function for the $n$th band at $k$. Here, spin Berry curvature for the $n$th band can be defined as

$$\Omega_{z,n}^s(k) = \Sigma_{n' \neq n} \frac{-2\,\mathrm{Im}[\langle \psi_{nk}|\hat{j}_x^z|\psi_{n'k}\rangle\langle\psi_{n'k}|\hat{v}_y|\psi_{nk}\rangle]}{(E_n - E_{n'})^2}, \tag{4}$$

where $\hat{j}_x^z$ is the spin-current operator ($\hat{j}_x^z = \frac{1}{2}\{\hat{s}_z, \hat{v}_x\}$, with $\hat{s}_z = \hbar\hat{\sigma}/2$ as the spin operator and $\hat{v}_x$ as the velocity operator) [15,49].

## III. RESULTS AND DISCUSSION

### A. Crystal symmetry and effect of SOC on band structure

As proposed in our previous work [32], the puckered single-ayer tellurene exists in two different monoclinic phases having space groups $P2/m(10)$ ($\beta$-Te) and $P2(3)$ ($\beta'$-Te). Tellurene is multivalent in nature, and structurally Te-atoms are covalently bonded to each other with coordination numbers 3 and 4. Upon geometry optimization, $\beta$-Te acquires lattice constants $a = 5.69$ Å, $b = 4.22$ Å, and $c = 4.12$ Å similar to the earlier reported values [33]. The predicted stable $\beta'$-Te has lattice parameters $a = 5.96$ Å and $b = 4.51$ Å in two dimensions [32]. It can be obtained by exfoliating bulk-Te using mechanical or chemical means, wherein 1D Te helical chains are stacked and weakly coupled by van Der Waals forces. On reducing the dimension, $\beta'$-Te attains the monoclinic lattice from the trigonal bulk-Te. Tellurene monolayer is spatially inversion symmetric in $\beta$-Te, whereas it lacks inversion symmetry in $\beta'$-Te phase as shown in Fig. 1(a). The dissimilar Te-Te bond lengths on either side of the plane passing through center of inversion in $\beta'$-Te determines the existence of non-centrosymmetry in the system. This inversion asymmetry is at the core of inducing various structural-dependent properties that have been discussed in this paper.

Tellurene can undergo phase transitions between $\beta$ ($P2/m$) and $\beta'$ ($P2$) by controlling the strain in lattice parameters "$a$" and "$b$" as shown in Fig. 1(b), which represents the variation in area and lattice parameters with respect to strain. Blue dotted lines represent the parameters "$a$" and "$b$" of $\beta$-Te, while the solid lines are for the lattice parameters of $\beta'$-Te. Under the effect of strain, lattice parameter "$a$" of $\beta$-Te and $\beta'$-Te follow the same line but lattice parameter "$b$" of $\beta'$-Te follows a parallel line to that of $\beta$-Te. The biaxial strain applied to parameters in $\beta'$-Te from $-8\%$ to $+8\%$ is equivalent to $-3.6\%$ to $+13\%$ in $\beta$-Te. At 4.5% biaxial strain, $\beta$ loses its centrosymmetry and undergoes a phase transition from $P2/m$ to $P2$, that is, transits to $\beta'$-Te. $\beta$-Te can have a maximum area of $26.26 \times 10^{-16}$ cm$^2$ while $\beta'$-Te can have a minimum area of $24 \times 10^{-16}$ cm$^2$. For the smaller lattice parameters and area, $\beta$-Te is dominating, while for larger parameters and area, $\beta'$-Te is dominating. However, a small

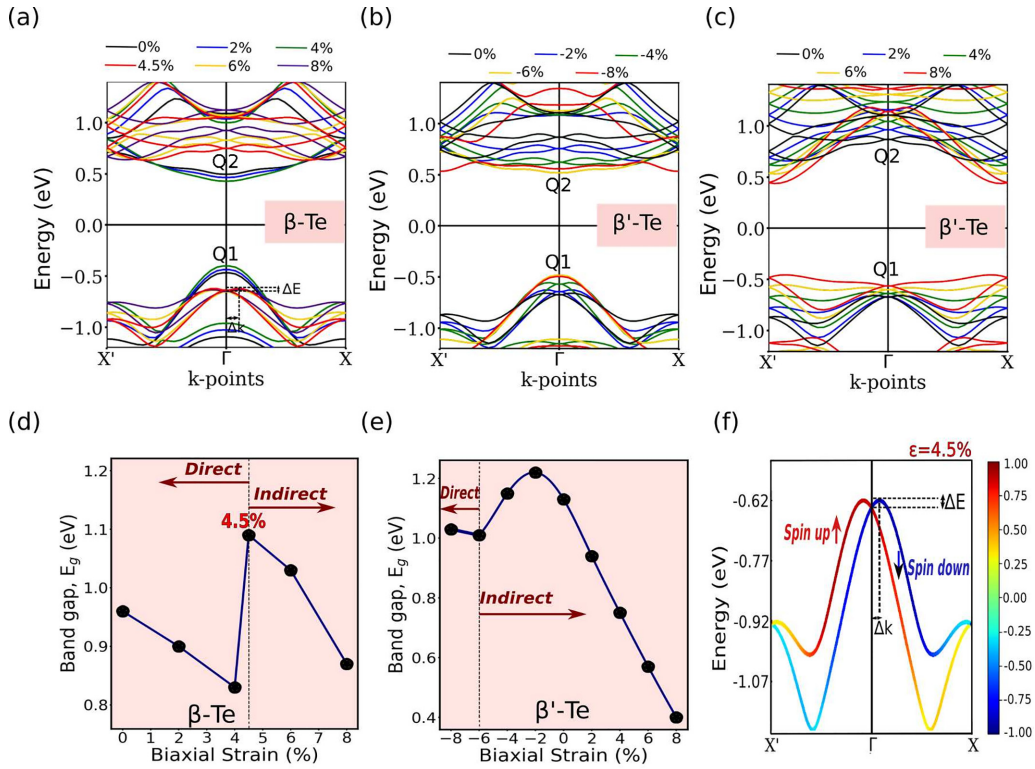


FIG. 2. Alteration in the band structures of (a) $\beta$-Te and (b),(c) $\beta'$-Te by applied biaxial strain in the range of 0–8 % and $-8\%$ to 8%, respectively, along the path $X'$-Γ-$X$. Strain leads to Rashba-type spin-splitting in the bands by generating noncentrosymmetry in tellurene. Q1 and Q2 represent the Rashba spin-splitting in the top valence and bottom conduction bands, respectively. (d) and (e) Variation in PBE-SOC calculated direct and indirect band gaps of $\beta$-Te and $\beta'$-Te by applied biaxial strain. (f) Spin-resolved top valence band showing Rashba spin splitting for 4.5% strained $\beta$-Te. Red and blue in the colorbar represent spin-up and spin-down states. Rashba energy splitting, $\Delta E$, and the corresponding momentum shift, $\Delta k$, are the Rashba parameters.

region of coexistence of both phases is found. This is because $\beta'$-Te is noncentrosymmetric from $-5.5\%$ to $+10\%$ biaxial strain [32]. So, here the combination of small parameters for compressive biaxial strain in $\beta'$-Te from $-5.5\%$ to 0% corresponds to the biaxial strains of $\sim -1\%$ to 4.5% in $\beta$-Te, and an overlapping region is obtained. Moreover, $\beta'$ phase with specific lattice parameters $a = 5.96$ Å and $b = 4.51$ Å has area $= 26.87 \times 10^{-16}$ cm$^2$. It can be seen lying in the explicit region of noncentrosymmetric space group P2 (lattice parameters are marked with green stars and area is marked with a green circle). So, the applied strain of $+4.7\%$ in "$a$" and $+6.8\%$ in "$b$" to $\beta$-Te results in $\beta'$-Te.

The electronic band structures for $\beta$-Te and $\beta'$-Te are shown in Figs. 1(c) and 1(d) for the closed path $Y$-Γ-$X$-$A$-$Y$ with SOC inclusion. The high-symmetry $k$ points are displayed in the Brillouin zone of a monoclinic lattice [Fig. 1(a)]. These spin-resolved band structures show contributed spin states. The obtained band structures using QUANTUM ESPRESSO completely resemble the electronic bands obtained earlier using VASP [32]. The contributions of spin-up and spin-down states in the band are observed in red and blue, respectively. In $\beta$-Te, degenerate spin states exist without any band splitting in it due to the presence of centrosymmetry. On the other hand, we observe the bands being split and procuring opposite spins in $\beta'$-Te under the effect of spin-orbit coupling. SOC produces band splitting with spin-polarized states for asymmetric materials [50]. Also, tellurene is a high atomic number element ($Z = 52$), and therefore it possesses large SOC ($E_{\mathrm{SOC}} \propto Z^4$). This kind of spin splitting in electronic states is significant for spin-based application, and it will be discussed in detail in the next section.

### B. Effect of strain on electronic properties

Various intriguing properties of 2D materials such as optical, thermoelectric, spintronic, and valleytronic properties are related to their electronic energy-momentum dispersion relation. These electronic properties are sensitive to the applied strain. So, it becomes important to investigate the modulation in electronic band structures due to external strain. A dilating biaxial strain is applied to $\beta$-Te in the range of 0–8 %. This strain range is chosen in alignment with our earlier report [32]. Figure 2(a) presents the alteration in band structures along the high-symmetry $k$ points $X'$-Γ-$X$ triggered by strain. The valence-band maxima (VBM) and conduction-band minima (CBM) of $\beta$-Te lie at the Γ-point indicating the presence of a direct band gap. The deformation in geometry from 0% to 4% does not affect the band characteristic or shape of the valence and conduction valleys. But small drifting of VBM and CBM valleys towards each other with increasing strain from 0% to 4% is spotted. At 4.5% applied strain, the inversion symmetry breaks and the crystal structure transits from centrosymmetric to noncentrosymmetric [as shown in Fig. 1(b)] that is, $\beta$-Te transits into $\beta'$-Te. This is confirmed by the change observed

in the band structure, that is, band splitting at valence and conduction valleys around the Γ-point at 4.5% strain (in red) shown in Fig. 2(a). As referred to in the previous section, SOC plays a crucial role in generating band splittings in broken inversion symmetry materials. The structure remains noncentrosymmetric at increasing strains, and accordingly a similar kind of band splitting is evident in the band structure at applied 6% and 8% strains.

Figures 2(b) and 2(c) displays the strain modulated bands of $\beta'$-Te for the path $X'$-Γ-$X$ within energy range −1.2 to 1.5 eV around Fermi energy. Herein, the variation in electronic properties is observed for strain values −8% to 0% in Fig. 2(b) and for 0–8 % in Fig. 2(c). As $\beta'$-Te is inversion asymmetric, split bands or split local VBM/CBM valleys exist at Γ-point for this indirect-band-gap material. However, vanishing band splitting is observed in electronic band structure under applied −6% and −8% strains, as can be seen in Fig. 1(b), where $\beta'$-Te transits back to $\beta$-Te. This is because of the acquirement of centrosymmetry by the structure. This type of phase transition does not occur under mechanical strains ranging from −4% to 8%, although drifting of bands and changes in band curvature are visible. It should be noted that bands are symmetrical for $\Gamma \rightarrow X'$ and $\Gamma \rightarrow X$ directions at all strains. Due to significant band evolution such as drifting and splitting of valleys by applied strain in $\beta$-Te as well as $\beta'$-Te, a strong strain-valley coupling is found to exist in these structures caused by geometrical distortion.

Strain-induced valley drifting leads to variation in band gap of $\beta$-Te [Fig. 2(d)] and $\beta'$-Te [Fig. 2(e)]. VBM and CBM valleys drift and approach each other for $\beta$-Te under 2% and 4% strain and thereby reduce the direct band gap by 60 and 130 meV, respectively. The direct-to-indirect crossover of the band gap occurs at 4.5% strain, and again with increasing strain, the band-gap reduction happens by 60 meV at 6% strain and by 220 meV at 8% strain. Looking into the band-gap evolution of $\beta'$-Te with strain, the direct-to-indirect crossover is seen at −6% value of strain. The largest indirect band gap of 1.22 eV occurs at −2% strain and the band gap goes as small as 400 meV at 8% strain. The direct-to-indirect band-gap transition is directly correlated to the phase transition in tellurene monolayers.

The band splitting observed at the local valence-band maxima and conduction-band minima at the Γ-point in tellurene monolayers (Fig. 2) is a Rashba-type spin splitting. The enlarged view of 4.5% strained $\beta$-Te is shown in Fig. 2(f) for the clear demonstration of the Rashba effect in single-layer tellurene. The two split bands possess opposite spins, that is, spin up (in red) and spin down (in blue) along the high-symmetry path $X'$-Γ-$X$. This is the SOC-induced Rashba spin splitting and is described by the Hamiltonian [50]

$$H_R = -\alpha_R \sigma \times \mathbf{k} \cdot \hat{r}, \tag{5}$$

where $\alpha_R$ is the Rashba strength coefficient, $\sigma$ is the Pauli spin matrix vector, $k$ is the momentum vector, and $r$ is the direction of intrinsic electric field. This electric field is produced by the potential gradient, which is caused by the asymmetry in the crystal structure of material. So, the two foremost conditions governing the occurrence of Rashba electronic states are the broken inversion symmetry and the presence of strong spin-orbit coupling in the material. The Rashba coefficient determines the strength of spin-momentum locking in the electronic band structure and is quantified as

$$\alpha_R = \frac{2\Delta E_R}{\Delta k_R}, \tag{6}$$

where $\Delta E_R$ is the energy splitting between the two bands, and $\Delta k_R$ is the corresponding momentum shift. These Rashba parameters are depicted in Fig. 2(f).

Further, the energy splitting, momentum shift, and Rashba coefficient are calculated for tellurene under different amounts of applied strain as shown in Fig. 3. The spin-splitting energies of SOC-induced Rashba at the Γ-point valence bands in $\beta$-Te monolayer vary from 16 to 14.4 meV for strains 4.5–8 % and the corresponding momentum shift variation is small, as seen in Figs. 3(a) and 3(b). The obtained Rashba coefficients from these entities reduce slightly from 0.58 to 0.535 eV Å with increasing tensile strain. Simultaneously, variation in Rashba parameters of conduction bands is also studied. Energy splitting, momentum shift, and the resulting Rashba coefficients are higher in conduction bands than the valence bands. Also, the Rashba coefficient increases with the applied tensile strain from 0.82 eV Å at 4.5% to 0.9 eV Å at 8%. Figures 3(d)–3(f) show the variation of Rashba parameters of $\beta'$-Te with strain. Rashba spin splitting is obtained both in valence and conduction bands in $\beta'$-Te. The Rashba constant in valence bands falls at 0% strain in $\beta'$-Te due to a decrease in energy splitting and an increase in momentum offset value. The eventual increase in both energy splitting and momentum shift of the valence bands with tensile strain results in a constant Rashba coefficient with slight variations. Also, it can be seen that larger SOC Rashba splitting occurs in conduction bands than valence bands of $\beta'$-Te under tensile strain from 0% to 8%. The Rashba constant ($\alpha_R$) goes as high as 1.09 eV Å in the valence band at −2% and reaches a maximum of 1.55 eV Å in the conduction band at 8%. This is due to more energy splitting and less momentum shift in the conduction bands, specifically at 8%. The Rashba coefficient is enhanced by two times at −2% and by three times at 8% strain in comparison to the unstrained $\beta'$-Te. Thus, application of in-plane strain can be an effective method to tune the Rashba effect in the monolayers.

Microscopically, strain tunes the intrinsic electric field present in the 2D sheet. Strain causes structural changes that displace the charges, which in turn alters the electric field in the 2D sheet. The electric field upon interacting with spin-orbit coupling induces Rashba-type spin splitting in the electronic bands of tellurene monolayer. The emergence of the Rashba effect in $\beta$-Te by applied strain was suggested by Cai *et al.* [51].

The calculated Rashba coefficient of strained single-layer $\beta$-Te (0.58 eV Å) in valence bands is found to be comparable to the value of 0.5 eV Å of Janus MoSeTe [52]. In comparison, the determined Rashba of $\beta'$-Te at conduction bands under 8% strain (1.55 eV Å) is nearly 1.7 times the maximum Rashba constant of strained $\beta$-Te (0.90 eV Å at 8%) in conduction bands. Han *et al.* [53] calculations reveal the Rashba effect in CBM of 1D helical Te-chain, and by strain engineering the authors have been successful in enhancing the Rashba constant from 0.84 to 2.17 eV Å at a high strain of 23%. On the other hand, 2D $\beta'$-Te monolayer attained a giant Rashba

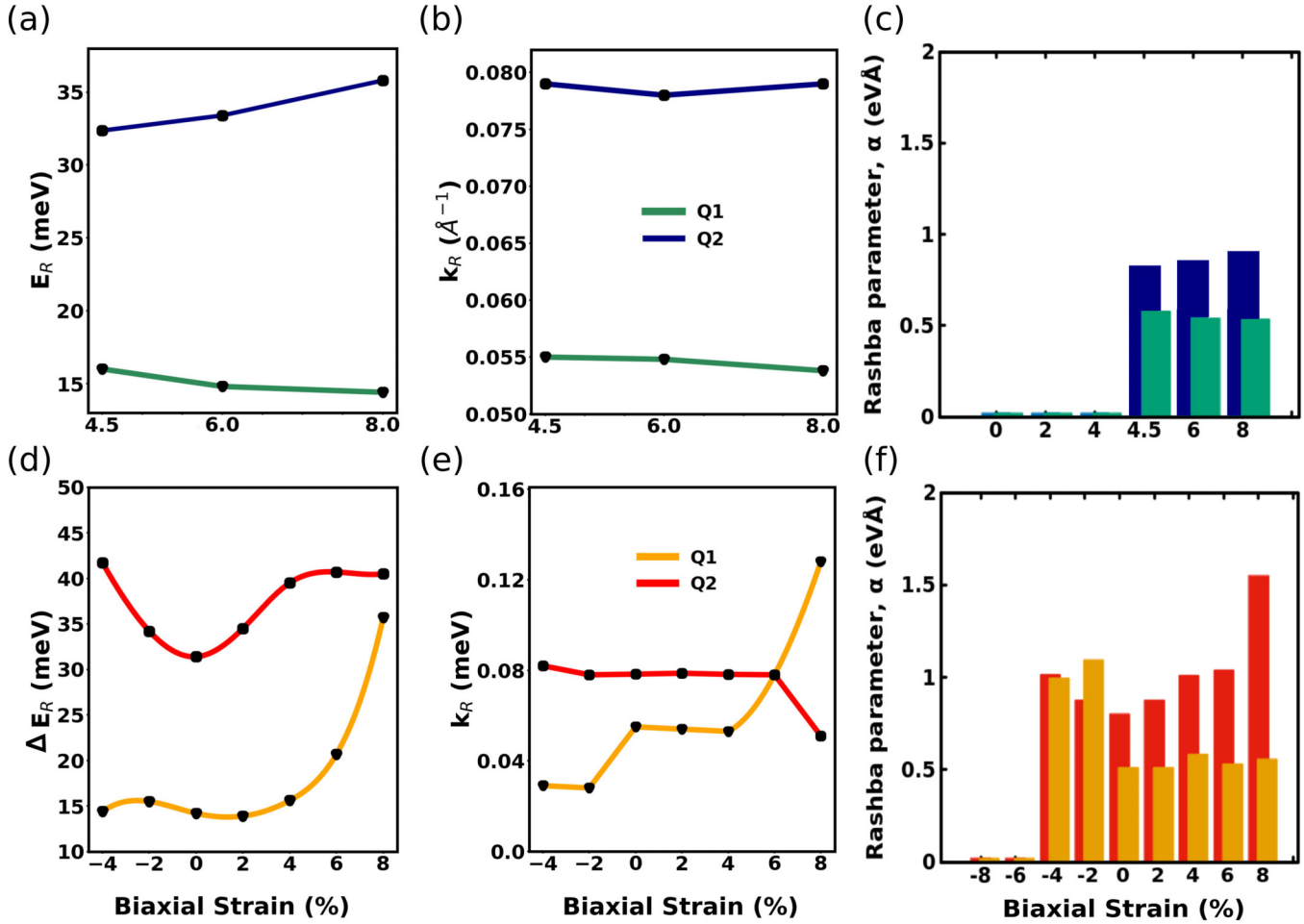


FIG. 3. The calculated variation in Rashba energy splitting ($\Delta E_R$), momentum shifting ($\Delta k_R$), and Rashba parameter ($\alpha_R$) of (a)–(c) $\beta$-Te and (d)–(f) $\beta'$-Te monolayers by biaxial strain.

strength of 1.55 eV Å at a comparatively smaller strain of 8%. Reportedly, other 2D materials like Janus WSTe, WSeTe, and MoSeTe have significant Rashba spin splitting at the valence bands with coefficients as 0.32, 0.51, and 0.50 eV Å, respectively [52,54]. Hu *et al.* [52] also showed that strain can modulate Rashba constants of these Janus TMDCs and can increase the constant to 1.1 eV Å for MoSeTe at −3% strain. These materials have Rashba strength larger at the valence bands than conduction bands. Janus MoSSe is reported to have a very small Rashba constant of 0.06 eV Å and it further reduces with increasing tensile biaxial strain [52,55]. Besides TMDCs, group III 2D monochalcogenides have considerable Rashba splitting in conduction bands with Rashba coefficients of 0.5 and 0.45 eV Å for GaTe and InTe, respectively [56]. Lee *et al.* [50] estimated a large value of Rashba splitting (2.16 eV Å) in conduction bands of $Si_2Bi_2$ monolayer. Moreover, $\beta$-Te and $\beta'$-Te have Rashba parameters higher than the metal surfaces such as 0.33 eV Å of Au(111) surface [57] and 0.55 eV Å of Bi(111) surface [58]. Overall, tellurene monolayers have values of Rashba coefficient (modulated by strain) significantly large enough to be utilised in spintronic devices. These devices are generally fabricated from the *n*-type semiconductors, wherein electron spin is modulated and transported to transmit information. This indicated that the Rashba effect in conduction bands of materials is crucial. However, since the experimental verification of spin transport in *p*-type silicon at room temperature [59], the fact that hole spin can also transfer and store information reliably over a few nanometers is established. Therefore, large Rashba spin splitting in valence bands also becomes beneficial in spintronics, and hence spin of both electrons and holes in tellurene monolayers can be utilized to transfer spin-based information via a spin field-effect transistor (spin-FET) channel.

Analogous to the Rashba effect, spin-orbit coupling in conjunction with lattice inversion asymmetry leads to SOC spin splitting, which lifts the spin degeneracy in the bands. As discussed previously, the spin-polarized states are generated in the electronic bands of noncentrosymmetric materials by the inclusion of SOC. The specific split bands having opposite spins along the particular paths $\Gamma \rightarrow X$ in the top valence band and $\Gamma \rightarrow X$, $A \rightarrow Y$ in the lower conduction band in a noncentrosymmetric structure can be seen in Fig. 1(d). The amount of spin splitting has been computed for these bands, and modulation with compressive and tensile strains is shown in Fig. 4. Spatially inversion symmetric $\beta$-Te does not exhibit spin-split electronic states, but as soon as it undergoes a phase transition at 4.5% strain, SOC spin splitting is obtained as $\Delta_{v(\Gamma\text{-}X)}$, $\Delta_{c(\Gamma\text{-}x)}$, and $\Delta_{c(A\text{-}Y)}$ [Fig. 4(b)]. The

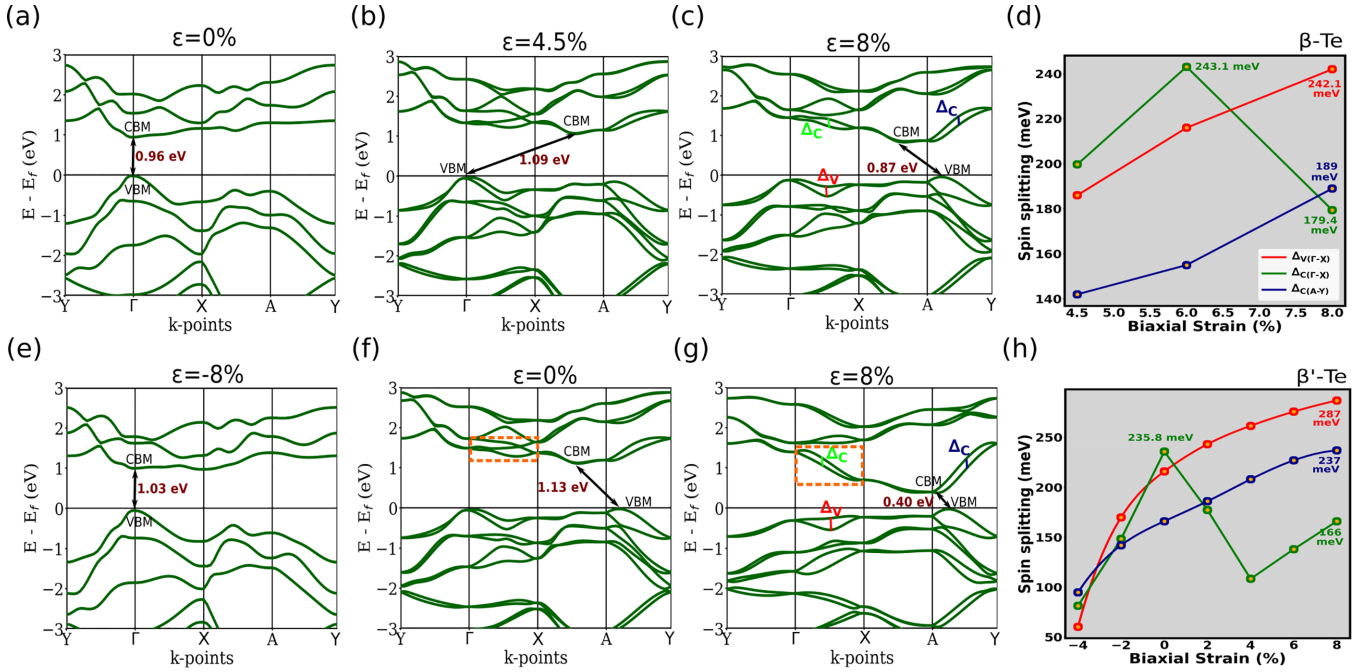


FIG. 4. Band-structure modulations for different values of biaxial strain in (a)–(c) $\beta$-Te and (d)–(f) $\beta'$-Te. Inversion symmetrized structures display the direct band gap ($E_g$) at the Γ-point, and structures with broken inversion symmetry have indirect band gaps [$E_g(\Gamma - XA)$, $E_{g(AY-BA)}$, $E_{g(AY-AY)}$]. $\Delta_v$ and $\Delta_c$ [shown in (g) and (h)] indicate the energy change in spin-split top valence and bottom conduction bands along the different $k$ points in $\beta$-Te and $\beta'$-Te. The orange dashed boxes depict the change in shape of the conduction band along Γ-$B$ for different strains. Parts (d) and (h) present the resulting large spin-split values in the range of 50–290 meV under different biaxial strains.

computed strain-controlled spin-split valence (VB) and conduction bands (CB) values are depicted in Fig. 4(g) for $\beta$-Te. $\Delta_{v(\Gamma\text{-}X)}$ and $\Delta_{c(A\text{-}Y)}$ acquire positive incremental slopes for strain ranging from 4.5% to 8% while $\Delta_{c(\Gamma\text{-}X)}$ displays a maximum spin splitting of 243.1 meV at 6% and falls to 179.4 meV at 8%.

Furthermore, opposite spin moments exist in the split bands of $\beta'$-Te by the incorporation of spin-orbit coupling in the broken inversion symmetric system. The fulfillment of both the conditions to obtain spin-split bands is essential. The absence of SOC does not lead to splitting of bands in the noncentrosymmetric $\beta'$-Te monolayer as observed in the earlier report [32]. The large intrinsic spin polarizations in the unstrained monolayer such as 215.9, 235.8, and 166.0 meV for $\Delta_{v(\Gamma\text{-}X)}$, $\Delta_{c(\Gamma\text{-}X)}$, and $\Delta_{c(A\text{-}Y)}$, respectively, are due to large SOC in tellurene. These spin-splitting values further amplify to 287 and 237 meV for $\Delta_{v(\Gamma\text{-}X)}$ and $\Delta_{c(A\text{-}Y)}$, respectively, with expansion in a 2D sheet while $\Delta_{c(\Gamma\text{-}X)}$ follows a decreasing-increasing trend under tensile strain [Fig. 4(h)]. The compressive strains from 0% to −4% lead to a decrease in all three spin splittings. The variation in strain-controlled spin splitting comes from the corresponding variations in the band structure with strain. The change in characteristic shape of the split conduction band (Γ-$X$) has been highlighted by dashed boxes in Fig. 4. The repositioning of VBM and CBM due to applied strain is also visible.

The above analysis shows that tellurene monolayers have huge strain-tunable spin splittings in the valence and conduction bands. The large spin splittings in bands imply a large energy difference between the two nondegenerate spin states. This suppresses the intervalley and spin-flip scattering and thus allows to retain the spin-based information reliably for a relatively longer time with large spin lifetimes [60]. Strained $\beta$-Te and $\beta'$-Te have spin splittings as high as 243.1 meV (in the CB) and 287 meV (in the VB), which are large in comparison to 2D materials like $MoS_2$ (150 meV, VBM), $MoSe_2$ (180 meV, VBM), MoSSe (170 meV, VBM and 13.7 meV, CBM), and $VSi_2N_4$ (102.3 meV, VBM and 27.3 meV, CBM) [15,55,61,62]. Tellurene is found to have quite a large energy difference in the alternate spin orientations of VB as well as CB. Such giant spin splittings in the valence and conduction bands are remarkable and significant for spintronic applications.

The broken inversion symmetry introduces another geometry-based feature in tellurene known as valley contrasting Berry curvature. It emerges from the existence of inequivalent valleys in the momentum space. Tellurene is found to have energy-degenerate valence and conduction bands along Γ-$X$ and Γ-$X'$ as shown in Fig. 2. These momentum-inequivalent top valence bands and lower conduction bands have opposite spins in both $\Gamma \rightarrow X$ and $\Gamma \rightarrow X'$ directions. Figure 2(f) depicts this opposite spin occupation in the momentum inequivalent valence bands. The spin moments in momentum inequivalent conduction bands are alternative to the ones present in valence bands. This implies the existence of spin-valley coupling in tellurene, where energy-degenerate but inequivalent valleys or valence and conduction bands can be distinguished by the spin of carriers. Time-reversal symmetry is responsible for the acquisition of these opposite spin splittings in momentum inequivalent bands [1,15]. Furthermore, TR symmetry in spatial inversion asymmetric tellurene leads to opposite Berry curvature along $\Gamma \rightarrow X$ and

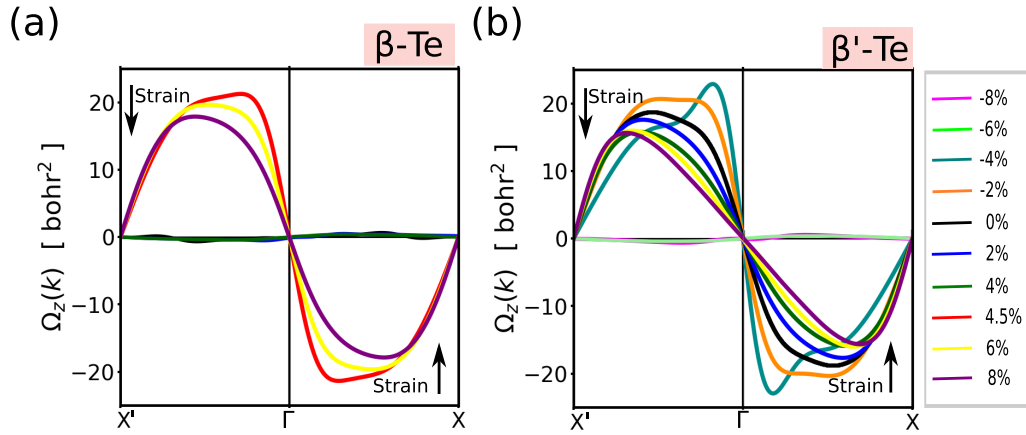


FIG. 5. Berry curvature $\Omega_z(k)$ of (a) $\beta$-Te and (b) $\beta'$-Te monolayers along $k$ points $X'$-$\Gamma$-$X$ under the application of variable biaxial strain values.

$\Gamma \rightarrow X'$ as presented in Fig. 5. The effect of biaxial strain on the Berry curvature of $\beta$ and $\beta'$ phases has been studied. Figure 5 represents the distribution of out of plane BC, $\Omega_z(k)$ along the high-symmetry $k$-path at various strains which is symmetric about the $\Gamma$-point [$\Omega_z(-k) = -\Omega_z(k)$] according to TR symmetry. Figure 5(a) shows zero Berry curvature in $\beta$-Te for applied strain from 0% to 4%. At 4.5% strain, the phase transition leads to Berry curvature having large magnitude of 21.27 Bohr$^2$. The peaks of Berry curvature are opposite along the $k$ paths $\Gamma \rightarrow X$ and $\Gamma \rightarrow X'$. Here, the inversion symmetry breaking leads to high polarization or piezoelectricity in the monolayer [32] and thereby large Berry curvature is obtained. Similarly, Kim *et al.* [63] has reported the emergence of ferroelectricity driven Berry curvature in SnTe. Here, the BC magnitude decreases with increasing tensile strain from 21.27 Bohr$^2$ (4.5%) to 17.90 Bohr$^2$ (8%). Additionally, the movement of broad BC peaks is evident from $\Gamma$ towards $X$ (or $X'$) with increasing biaxial dilating strain. Next, the obtained Berry curvatures for $\beta'$-Te under strain [Fig. 5(b)] are analyzed. Here, the maximum obtained value of BC is 22.90 Bohr$^2$ at $-4\%$ compressive strain and it decreases to 15.66 Bohr$^2$ at 8% accompanied with the drifting of peak towards $X$ (or $X'$). The strain modified Berry curvature in tellurene is comparatively smaller than the BC of $\sim$60 Bohr$^2$ in $MoS_2$ [15]. Janus MoSSe monolayer has $\Omega_z(k)$ close to 50 Bohr$^2$ while it gets doubled upon constructing the bilayer [64]. Tungsten-based materials such as $WS_2$ on a MnO substrate has a Berry curvature of approximately 60 Bohr$^2$ [65] and $WN_2F_2$ has value equivalent to 68.33 Bohr$^2$ [66].

### C. Strain manipulated spin Hall conductivity

The dynamics of Berry curvature influence the valley-related transport properties. The carriers gain anomalous velocities to move in opposite time-reversal connected valleys due to the intrinsic in-plane electric field ($E$) according to the expression $\mathbf{v} = -\frac{e}{\hbar}\mathbf{E} \times \mathbf{\Omega_z}(k)$, where $\mathbf{v}$ is the transverse velocity perpendicular to both the in-plane electric field and out-of-plane Berry curvature. The flow of carriers in opposite valleys corresponds to the valley Hall effect in which the carrier movement can be controlled by external optical or magnetic means to get unequal concentration in the two valleys. The Hall effect is normally realized in a material under external magnetic field while the anomalous Hall effect is observed in ferromagnetic materials induced due to intrinsic magnetic moments. Tellurene is a nonmagnetic material with the occurrence of valley-dependent Berry curvature in it which bluffs as the effective magnetic field in the momentum space. The presence of time-reversal symmetry and opposite Berry curvature valleys in tellurene lead to equal and opposite transverse charge current in the momentum-inequivalent valleys. This results in net zero anomalous Hall conductivity in tellurene monolayer. Tellurene exhibits another transport phenomenon, that is, the intrinsic spin Hall effect. This effect owes its origin to the strong spin-orbit coupling and is governed by spin Berry curvature [shown in Fig. 6(a)]. Spin Berry curvature (SBC) follows $\Omega_z^s(k) = \Omega_z^s(-k)$ and remains unchanged under the effect of time-reversal symmetry as both $s_z$ and $\Omega_z(k)$ reverse for $t \rightarrow -t$. So, $\Omega_z^s(k)$ has the same sign for broad peaks in $\Gamma \rightarrow X$ and $\Gamma \rightarrow X'$ directions. The spin Hall conductivities (SHC) governed by spin Berry curvature are computed using Eq. (3) (in Sec. II) and plotted as a function of Fermi energy and strain in Fig. 6(b) for $\beta'$-Te. The actual Fermi level is set at the zero of VBM and SHC and is determined at varying Fermi energies. As $\beta'$-Te possesses broken inversion symmetry, spin Berry curvature-induced spin transport is attained in it. The maximum SHC $\sigma_{xy}^{\mathrm{SHC}} \sim 44(\hbar/e)$ S/cm is obtained at hole doping, $n_h$ of $1.1 \times 10^{15}$ cm$^{-2}$. Doping of the order of $10^{13}$ cm$^{-2}$ around the VBM and the CBM is easily attainable. So, the variation of SHC with strain is presented in the inset of Fig. 6(b) for both electron concentration $n_e = 2.3 \times 10^{13}$ cm$^{-2}$ and hole concentration $n_h = 1.1 \times 10^{15}$ cm$^{-2}$. Figure 6(b) (inset) shows that compressive and tensile strains decrease the magnitude of spin Hall conductivity in $\beta'$-Te at the specific hole concentration. At $n_e \sim 10^{13}$ cm$^{-2}$, the magnitude of SHC is highest at $-6\%$ [$-18.26(\hbar/e)$ S/cm] and undergoes a slight increment from 3.68 $(\hbar/e)$ S/cm to 5.652 $(\hbar/e)$ S/cm under tensile strains. Hence, intrinsic SHC can be tuned by the simultaneous control of strain and doping in tellurene.

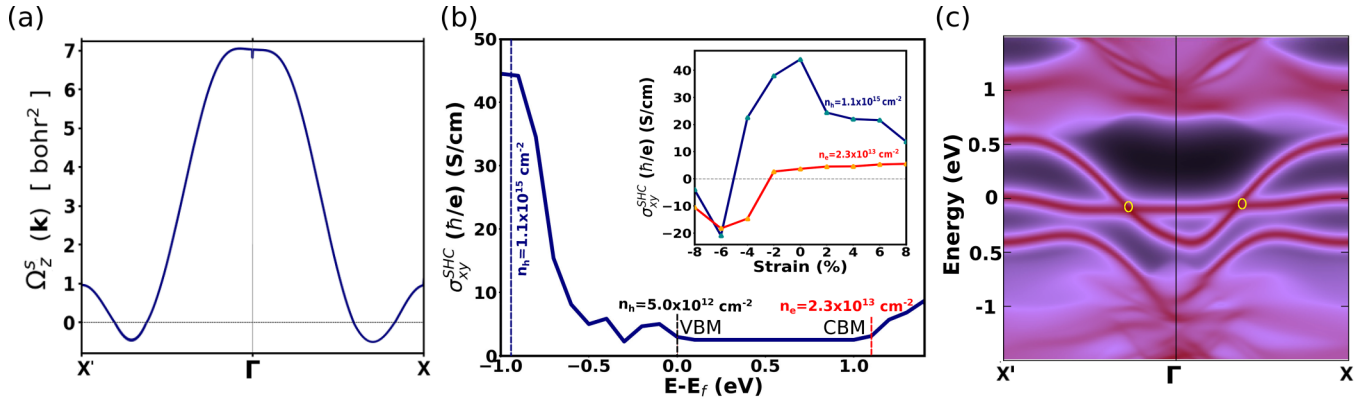


FIG. 6. (a) Spin Berry curvature of $\beta'$-Te. (b) Variation of spin Hall conductivity as a function of Fermi energy and biaxial strain in $\beta'$-Te monolayer. (c) Calculated edge state band structure for $\beta'$-Te, presenting two pairs of crossing edge states.

Comparatively, SHC of 44 $(\hbar/e)$ S/cm in $\beta'$-Te at $n_h = 1.1 \times 10^{15}$ cm$^{-2}$ is equivalent to the SHC value in GeS [43$(\hbar/e)$ S/cm] [31] and higher than $PtTe_2$ bilayer with different stackings [$AA \sim -8.41$ $(\hbar/e)$ S/cm and $AB \sim 27.28$ $(\hbar/e)$ S/cm] [17]. For easy comparison, SHC of $\beta'$-Te can be written as 0.28 $(e^2/h)$ at $n_h = 1.1 \times 10^{15}$ cm$^{-2}$ and 0.023 $(e^2/h)$ at $n_e = 2.3 \times 10^{13}$ cm$^{-2}$, respectively. SHC at the mentioned electron concentration is comparable to $1T'$-$MoS_2$ $[-0.018(e^2/h)]$ but somewhat smaller than $1T'$-$WS_2$ $[0.044(e^2/h)]$, $1S$-$MoS_2$ $[0.86(e^2/h)]$, and $1S$-$WS_2$ $[0.89(e^2/h)]$ [67]. Monoelemental germanene and stanene also exhibit higher spin Hall conductivities of $\sim$0.98 $(e^2/h)$ [67]. Feng *et al.* [15] reported the spin Hall conductivity in hexagonal phases of TMDCs such as $MoS_2[-0.036(e^2/h)]$, $MoSe_2[-0.057(e^2/h)]$, $WS_2[-0.071(e^2/h)]$, and $WSe_2[-0.081(e^2/h)]$ at hole doping of $1 \times 10^{13}$ cm$^{-2}$. At this doping concentration, SHC in $\beta'$-Te is smaller than these TMDCs.

In the band-gap region, $\beta'$-Te has a constant SHC value of 2.48 $(\hbar/e)$ S/cm without any charge current. Murakami *et al.* [68] suggested the presence of nonzero spin Hall conductivity in gapped semiconductors such as Pb$X$ ($X$ = S, Se, Te) at zero doping (band-gap region) and termed such semiconductors as spin Hall insulators. Ma *et al.* [69] predicted 2D penta-Sn$X_2$ ($X$ = S, Se, Te) as the quantum spin Hall insulator with large band gaps. Similarly, Qian *et al.* [26] reported $1T'$-$MX2$ TMDCs as large gap quantum spin Hall insulators. Feng *et al.* [15] demonstrated finite values of SHC in the band gap of bulk as well as monolayers of $WS_2$ and $WSe_2$. In a recent report, $\alpha$ phase of tellurene has been experimentally reported as a 2D topological insulator by Khatun *et al.* [70] Also, the bulk trigonal tellurium consisting of 1D helical chains is reportedly a 3D topological insulator under strain conditions [71]. One of the possible reasons for nonzero SHC in the forbidden region in $\beta'$-Te is the presence of nontrivial band structure with crossing spin edge states in the gapped region. This has been confirmed by the edge state band-structure calculation for $\beta'$-Te as shown in Fig. 6(c), wherein two pairs of helical edge states can be seen crossing in the nontrivial gap. So, $\beta'$-Te has an insulating bulk band gap and conducting edge states that are topologically protected due to the time-reversal symmetry. Therefore, $\beta'$-Te exhibits a double quantum spin Hall effect (QSHE) in comparison to the conventional QSHE where a single pair of gapless edge states exists. Recently, Bai *et al.* [28] reported a double quantum spin Hall effect in $\alpha$-Sb and $\alpha$-Bi. $\beta'$-Te has the advantage of having a large band gap, as the small band gaps in spin Hall insulators limit its operating regime to low temperatures. Also, a large band gap results in efficient switching between ON and OFF states. So, tellurene can be employed in low power quantum electronics.

## IV. CONCLUSION

In summary, spin-valley coupling modulated by strain has been demonstrated in tellurene monolayers in view of large valley and spin splittings. Tellurene harbors valley-dependent Berry curvature, which is observed in centrosymmetric $\beta$-Te via phase transition under the effect of strain. Precisely, biaxial strain of 4.5% breaks the inversion symmetry in $\beta$-Te, and consequently a large BC of 21.27 Bohr$^2$ and a Rashba coefficient of 0.90 eV Å are achieved. BC of $\beta'$-Te has a maximum value of 22.90 Bohr$^2$ at $-4$% compressive strain. A large Rashba coefficient of 1.55 eV Å is obtained at 8% strain in $\beta'$-Te. Both $\beta$ and $\beta'$ phases acquire significantly large SOC spin splittings tunable by strain higher than Mo$X_2$ ($X$ = S, Se, Te). Additionally, the inherent tellurene spin Hall effect is managed by the external factors of biaxial strain and doping. $p$-type $\beta'$-Te exhibits a high SHC of 44 $(\hbar/e)$ S/cm at $n_h \approx 1.1 \times 10^{15}$ cm$^{-2}$, and $n$-type $\beta'$-Te exhibits SHC of 3.68 $(\hbar/e)$ S/cm at $n_e \approx 2.3 \times 10^{13}$ cm$^{-2}$. Also, nonzero SHC of 2.48 $(\hbar/e)$ S/cm is obtained in the band-gap region in $\beta'$-Te, which indicates tellurene as a potential spin Hall insulator. $\beta'$-Te has insulating bulk and two pairs of conducting helical edge states indicating the presence of a double quantum spin Hall effect in it. We put forward strain as an effective strategy to modulate the physical properties, and we propose piezoelectric Te as a self-powered spin-valleytronic material. Our results will enrich the understanding of strain coupled spin-valley physics occurring in monoclinic tellurene, and they will expand the range of spin-valleytronics materials beyond TMDCs.

## ACKNOWLEDGMENTS

P.K.S. acknowledges University Grants Commission, India for a PhD fellowship [Grant No. 3724/(NET-DEC2018)].

We acknowledge the financial support offered by DST-SERB, India (Grant No. EEQ/2016/00049). We are thankful to the in-house supercomputing facility at INST, Mohali.

[1] J. R. Schaibley, H. Yu, G. Clark, P. Rivera, J. S. Ross, K. L. Seyler, W. Yao, and X. Xu, Valleytronics in 2D materials, Nat. Rev. Mater. **1**, 16055 (2016).

[2] S. A. Vitale, D. Nezich, J. O. Varghese, P. Kim, N. Gedik, P. Jarillo-Herrero, D. Xiao, and M. Rothschild, Valleytronics: Opportunities, challenges, and paths forward, Small **14**, 1801483 (2018).

[3] H. Zeng, J. Dai, W. Yao, D. Xiao, and X. Cui, Valley polarization in $MoS_2$ monolayers by optical pumping, Nat. Nanotechnol. **7**, 490 (2012).

[4] K. F. Mak, K. He, J. Shan, and T. F. Heinz, Control of valley polarization in monolayer $MoS_2$ by optical helicity, Nat. Nanotechnol. **7**, 494 (2012).

[5] R. Peng, Y. Ma, S. Zhang, B. Huang, and Y. Dai, Valley polarization in Janus single-layer MoSSe via magnetic doping, J. Phys. Chem. Lett. **9**, 3612 (2018).

[6] C. Zhao, T. Norden, P. Zhang, P. Zhao, Y. Cheng, F. Sun, J. P. Parry, P. Taheri, J. Wang, and Y. Yang, Enhanced valley splitting in monolayer $WSe_2$ due to magnetic exchange field, Nat. Nanotechnol. **12**, 757 (2017).

[7] T. Norden, C. Zhao, P. Zhang, R. Sabirianov, A. Petrou, and H. Zeng, Giant valley splitting in monolayer $WS_2$ by magnetic proximity effect, Nat. Commun. **10**, 4163 (2019).

[8] I. Khan, B. Marfoua, and J. Hong, Electric field induced giant valley polarization in two dimensional ferromagnetic $WSe_2/CrSnSe_3$ heterostructure, npj 2D Mater. Appl. **5**, 10 (2021).

[9] B. Huang, G. Clark, E. Navarro-Moratalla, D. R. Klein, R. Cheng, K. L. Seyler, D. Zhong, E. Schmidgall, M. A. McGuire, and D. H. Cobden, Layer-dependent ferromagnetism in a van der Waals crystal down to the monolayer limit, Nature (London) **546**, 270 (2017).

[10] H. H. Kim, B. Yang, T. Patel, F. Sfigakis, C. Li, S. Tian, H. Lei, and A. W. Tsen, One million percent tunnel magnetoresistance in a magnetic van der Waals heterostructure, Nano Lett. **18**, 4885 (2018).

[11] W. Xiao, L. Xu, G. Xiao, L.-L. Wang, and X.-Y. Dai, Two-dimensional hexagonal chromium chalco-halides with large vertical piezoelectricity, high-temperature ferromagnetism, and high magnetic anisotropy, Phys. Chem. Chem. Phys. **22**, 14503 (2020).

[12] M. Bonilla, S. Kolekar, Y. Ma, H. C. Diaz, V. Kalappattil, R. Das, T. Eggers, H. R. Gutierrez, M.-H. Phan, and M. Batzill, Strong room-temperature ferromagnetism in $VSe_2$ monolayers on van der Waals substrates, Nat. Nanotechnol. **13**, 289 (2018).

[13] D. J. O'Hara, T. Zhu, A. H. Trout, A. S. Ahmed, Y. K. Luo, C. H. Lee, M. R. Brenner, S. Rajan, J. A. Gupta, and D. W. McComb, Room temperature intrinsic ferromagnetism in epitaxial manganese selenide films in the monolayer limit, Nano Lett. **18**, 3125 (2018).

[14] A. Gupta, H. Silotia, A. Kumari, M. Dumen, S. Goyal, R. Tomar, N. Wadehra, P. Ayyub, and S. Chakraverty, $KTaO_3$—the new kid on the spintronics block, Adv. Mater. **34**, 2106481 (2022).

[15] W. Feng, Y. Yao, W. Zhu, J. Zhou, W. Yao, and D. Xiao, Intrinsic spin Hall effect in monolayers of group-VI dichalcogenides: A first-principles study, Phys. Rev. B **86**, 165108 (2012).

[16] S. Husain, R. Gupta, A. Kumar, P. Kumar, N. Behera, R. Brucas, S. Chaudhary, and P. Svedlindh, Emergence of spin-orbit torques in 2d transition metal dichalcogenides: A status update, Appl. Phys. Rev. **7**, 041312 (2020).

[17] J. Li, H. Jin, Y. Wei, and H. Guo, Tunable intrinsic spin Hall conductivity in bilayer $PtTe_2$ by controlling the stacking mode, Phys. Rev. B **103**, 125403 (2021).

[18] S. Liang, H. Yang, P. Renucci, B. Tao, P. Laczkowski, S. Mc-Murtry, G. Wang, X. Marie, J.-M. George, S. P. Watelot *et al.*, Electrical spin injection and detection in molybdenum disulfide multilayer channel, Nat. Commun. **8**, 14947 (2017).

[19] K. Wu, J. Chen, H. Ma, L. Wan, W. Hu, and J. Yang, Two-dimensional giant tunable rashba semiconductors with two-atom-thick buckled honeycomb structure, Nano Lett. **21**, 740 (2021).

[20] Z. Wu, B. T. Zhou, X. Cai, P. Cheung, G.-B. Liu, M. Huang, J. Lin, T. Han, L. An, Y. Wang *et al.*, Intrinsic valley Hall transport in atomically thin $MoS_2$, Nat. Commun. **10**, 611 (2019).

[21] B. Zhou, Z. Li, J. Wang, X. Niu, and C. Luan, Tunable valley splitting and an anomalous valley Hall effect in hole-doped $WS_2$ by proximity coupling with a ferromagnetic $MnO_2$ monolayer, Nanoscale **11**, 13567 (2019).

[22] Y. Zhang, J. V. D. Brink, C. Felser, and B. Yan, Electrically tuneable nonlinear anomalous Hall effect in two-dimensional transition-metal dichalcogenides $WTe_2$ and $MoTe_2$, 2D Mater. **5**, 044001 (2018).

[23] K. Kang, T. Li, E. Sohn, J. Shan, and K. F. Mak, Nonlinear anomalous Hall effect in few-layer $WTe_2$, Nat. Mater. **18**, 324 (2019).

[24] S. Bhowal and S. Satpathy, Intrinsic orbital and spin Hall effects in monolayer transition metal dichalcogenides, Phys. Rev. B **102**, 035409 (2020).

[25] C. L. Kane and E. J. Mele, Quantum Spin Hall Effect in Graphene, Phys. Rev. Lett. **95**, 226801 (2005).

[26] X. Qian, J. Liu, L. Fu, and J. Li, Quantum spin Hall effect in two-dimensional transition metal dichalcogenides, Science **346**, 1344 (2014).

[27] S. Tang, C. Zhang, D. Wong, Z. Pedramrazi, H.-Z. Tsai, C. Jia, B. Moritz, M. Claassen, H. Ryu, and S. Kahn, Quantum spin Hall state in monolayer 1T'-$WTe_2$, Nat. Phys. **13**, 683 (2017).

[28] Y. Bai, L. Cai, N. Mao, R. Li, Y. Dai, B. Huang, and C. Niu, Doubled quantum spin Hall effect with high-spin Chern number in $\alpha$-antimonene and $\alpha$-bismuthene, Phys. Rev. B **105**, 195142 (2022).

[29] D. Xiao, G.-B. Liu, W. Feng, X. Xu, and W. Yao, Coupled Spin and Valley Physics in Monolayers of $MoS_2$ and Other Group-VI Dichalcogenides, Phys. Rev. Lett. **108**, 196802 (2012).

[30] J. Son, K.-H. Kim, Y. Ahn, H.-W. Lee, and J. Lee, Strain Engineering of the Berry Curvature Dipole and Valley Magnetization in Monolayer $MoS_2$, Phys. Rev. Lett. **123**, 036806 (2019).

[31] J. Sławińska, F. T. Cerasoli, H. Wang, S. Postorino, A. Supka, S. Curtarolo, M. Fornari, and M. B. Nardelli, Giant spin Hall effect in two-dimensional monochalcogenides, 2D Mater. **6**, 025012 (2019).

[32] P. K. Sachdeva, S. Gupta, and C. Bera, Large piezoelectric and thermal expansion coefficients with negative Poisson's ratio in strain-modulated tellurene, Nanoscale Adv. **3**, 3279 (2021).

[33] Z. Zhu, X. Cai, S. Yi, J. Chen, Y. Dai, C. Niu, Z. Guo, M. Xie, F. Liu, and J.-H. Cho, Multivalency-Driven Formation of Te-Based Monolayer Materials: A Combined First-Principles and Experimental Study, Phys. Rev. Lett. **119**, 106101 (2017).

[34] W. Wu, G. Qiu, Y. Wang, R. Wang, and P. Ye, Tellurene: Its physical properties, scalable nanomanufacturing, and device applications, Chem. Soc. Rev. **47**, 7203 (2018).

[35] Y. Wang, G. Qiu, R. Wang, S. Huang, Q. Wang, Y. Liu, Y. Du, W. A. Goddard, M. J. Kim, and X. Xu, Field-effect transistors made from solution-grown two-dimensional tellurene, Nat. Electron. **1**, 228 (2018).

[36] G. Kresse and J. Furthmüller, Efficiency of ab-initio total energy calculations for metals and semiconductors using a plane-wave basis set, Comput. Mater. Sci. **6**, 15 (1996).

[37] P. E. Blöchl, Projector augmented-wave method, Phys. Rev. B **50**, 17953 (1994).

[38] G. Kresse and D. Joubert, From ultrasoft pseudopotentials to the projector augmented-wave method, Phys. Rev. B **59**, 1758 (1999).

[39] J. P. Perdew, K. Burke, and M. Ernzerhof, Generalized Gradient Approximation Made Simple, Phys. Rev. Lett. **77**, 3865 (1996).

[40] M. Ernzerhof and G. E. Scuseria, Assessment of the Perdew–Burke–Ernzerhof exchange-correlation functional, J. Chem. Phys. **110**, 5029 (1999).

[41] P. Giannozzi, S. Baroni, N. Bonini, M. Calandra, R. Car, C. Cavazzoni, D. Ceresoli, G. L. Chiarotti, M. Cococcioni, and I. Dabo, QUANTUM ESPRESSO: A modular and open-source software project for quantum simulations of materials, J. Phys.: Condens. Matter **21**, 395502 (2009).

[42] A. A. Mostofi, J. R. Yates, Y.-S. Lee, I. Souza, D. Vanderbilt, and N. Marzari, Wannier90: A tool for obtaining maximally-localised Wannier functions, Comput. Phys. Commun. **178**, 685 (2008).

[43] G. Pizzi, V. Vitale, R. Arita, S. Blügel, F. Freimuth, G. Géranton, M. Gibertini, D. Gresch, C. Johnson, and T. Koretsune, Wannier90 as a community code: New features and applications, J. Phys.: Condens. Matter **32**, 165902 (2020).

[44] S. S. Tsirkin, P. A. Puente, and I. Souza, Gyrotropic effects in trigonal tellurium studied from first principles, Phys. Rev. B **97**, 035158 (2018).

[45] Q. Wu, S. Zhang, H.-F. Song, M. Troyer, and A. A Soluyanov, WannierTools: An open-source software package for novel topological materials, Comput. Phys. Commun. **224**, 405 (2018).

[46] Y. Yao, L. Kleinman, A. MacDonald, J. Sinova, T. Jungwirth, D.-S. Wang, E. Wang, and Q. Niu, First Principles Calculation of Anomalous Hall Conductivity in Ferromagnetic bcc Fe, Phys. Rev. Lett. **92**, 037204 (2004).

[47] G. Guo, Y. Yao, and Q. Niu, *Ab initio* Calculation of the Intrinsic Spin Hall Effect in Semiconductors, Phys. Rev. Lett. **94**, 226601 (2005).

[48] J. Qiao, J. Zhou, Z. Yuan, and W. Zhao, Calculation of intrinsic spin Hall conductivity by Wannier interpolation, Phys. Rev. B **98**, 214402 (2018).

[49] Y. Yao and Z. Fang, Sign Changes of Intrinsic Spin Hall Effect in Semiconductors and Simple Metals: First-Principles Calculations, Phys. Rev. Lett. **95**, 156601 (2005).

[50] S. Lee and Y.-K. Kwon, Unveiling giant hidden Rashba effects in two-dimensional $Si_2Bi_2$, npj 2D Mater. Appl. **4**, 45 (2020).

[51] X. Cai, Y. Ren, M. Wu, D. Xu, and X. Luo, Strain-induced phase transition and giant piezoelectricity in monolayer tellurene, Nanoscale **12**, 167 (2020).

[52] T. Hu, F. Jia, G. Zhao, J. Wu, A. Stroppa, and W. Ren, Intrinsic and anisotropic Rashba spin splitting in Janus transition-metal dichalcogenide monolayers, Phys. Rev. B **97**, 235404 (2018).

[53] J. Han, A. Zhang, M. Chen, W. Gao, and Q. Jiang, Giant Rashba splitting in one-dimensional atomic tellurium chains, Nanoscale **12**, 10277 (2020).

[54] J. Chen, K. Wu, H. Ma, W. Hu, and J. Yang, Tunable Rashba spin splitting in Janus transition-metal dichalcogenide monolayers via charge doping, RSC Adv. **10**, 6388 (2020).

[55] S.-B. Yu, M. Zhou, D. Zhang, and K. Chang, Spin Hall effect in the monolayer Janus compound MoSSe enhanced by Rashba spin-orbit coupling, Phys. Rev. B **104**, 075435 (2021).

[56] M. Ariapour and S. B. Touski, Strain engineering of spin and Rashba splitting in group-III monochalcogenide MX (M= Ga, In and X= S, Se, Te) monolayer, J. Magn. Magn. Mater. **510**, 166922 (2020).

[57] S. LaShell, B. McDougall, and E. Jensen, Spin Splitting of an Au(111) Surface State Band Observed with Angle Resolved Photoelectron Spectroscopy, Phys. Rev. Lett. **77**, 3419 (1996).

[58] Y. M. Koroteev, G. Bihlmayer, J. Gayone, E. V. Chulkov, S. Blügel, P. M. Echenique, and P. Hofmann, Strong Spin-Orbit Splitting on Bi Surfaces, Phys. Rev. Lett. **93**, 046403 (2004).

[59] E. Shikoh, K. Ando, K. Kubo, E. Saitoh, T. Shinjo, and M. Shiraishi, Spin-Pump-Induced Spin Transport in *p*-Type Si at Room Temperature, Phys. Rev. Lett. **110**, 127201 (2013).

[60] S. Guo, H. Zheng, Y. Wang, and J. Zhang, Achieving giant spin-orbit splitting in conduction band of monolayer $WS_2$ via n-p co-doping, AIP Adv. **9**, 075304 (2019).

[61] C. Cheng, J.-T. Sun, X.-R. Chen, H.-X. Fu, and S. Meng, Nonlinear Rashba spin splitting in transition metal dichalcogenide monolayers, Nanoscale **8**, 17854 (2016).

[62] X. Zhou, R.-W. Zhang, Z. Zhang, W. Feng, Y. Mokrousov, and Y. Yao, Sign-reversible valley-dependent Berry phase effects in 2D valley-half-semiconductors, npj Comput. Mater. **7**, 160 (2021).

[63] J. Kim, K.-W. Kim, D. Shin, S.-H. Lee, J. Sinova, N. Park, and H. Jin, Prediction of ferroelectricity-driven Berry curvature enabling charge- and spin-controllable photocurrent in tin telluride monolayers, Nat. Commun. **10**, 3965 (2019).

[64] F. Li, W. Wei, H. Wang, B. Huang, Y. Dai, and T. Jacob, Intrinsic electric field-induced properties in Janus MoSSe van der Waals structures, J. Phys. Chem. Lett. **10**, 559 (2019).

[65] L. Xu, M. Yang, L. Shen, J. Zhou, T. Zhu, and Y. P. Feng, Large valley splitting in monolayer $WS_2$ by proximity coupling to an insulating antiferromagnetic substrate, Phys. Rev. B **97**, 041405(R) (2018).

[66] K. Dou, Y. Ma, R. Peng, W. Du, B. Huang, and Y. Dai, Promising valleytronic materials with strong spin-valley coupling in two-dimensional $Mn_2X_2$ (M= Mo, W; X= F, H), Appl. Phys. Lett. **117**, 172405 (2020).

[67] F. Matusalem, M. Marques, L. K. Teles, L. Matthes, J. Furthmüller, and F. Bechstedt, Quantization of spin Hall conductivity in two-dimensional topological insulators versus symmetry and spin-orbit interaction, Phys. Rev. B **100**, 245430 (2019).

[68] S. Murakami, N. Nagaosa, and S.-C. Zhang, Spin Hall Insulator, Phys. Rev. Lett. **93**, 156804 (2004).

[69] Y. Ma, L. Kou, X. Li, Y. Dai, and T. Heine, Room temperature quantum spin Hall states in two-dimensional crystals composed of pentagonal rings and their quantum wells, NPG Asia Mater. **8**, e264 (2016).

[70] S. Khatun, A. Banerjee, and A. J. Pal, Nonlayered tellurene as an elemental 2D topological insulator: Experimental evidence from scanning tunneling spectroscopy, Nanoscale **11**, 3591 (2019).

[71] L. A. Agapito, N. Kioussis, W. A. Goddard III, and N. P. Ong, Novel Family of Chiral-Based Topological Insulators: Elemental Tellurium under Strain, Phys. Rev. Lett. **110**, 176401 (2013).